Dirac semimetal in β-CuI without surface Fermi arcs

Congcong Le[a,b,c], Xianxin Wu[d,1], Shengshan Qin[c,e], Yinxiang Li[c], Ronny Thomale[d], Fu-Chun Zhang[a,b], and Jiangping Hu[a,b,c,f,1]

[a]Kavli Institute of Theoretical Sciences, University of Chinese Academy of Sciences, Beijing 100190, China; [b]Chinese Academy of Sciences Center for Excellence in Topological Quantum Computation, University of Chinese Academy of Sciences, Beijing 100190, China; [c]Beijing National Laboratory for Condensed Matter Physics, Institute of Physics, Chinese Academy of Sciences, Beijing 100190, China; [d]Institute for Theoretical Physics and Astrophysics, Julius-Maximilians University of Würzburg, D-97074 Würzburg, Germany; [e]University of Chinese Academy of Science, Beijing 100049, China; and [f]Collaborative Innovation Center of Quantum Matter, Beijing 100049, China

Edited by Siddharth Parameswaran, Oxford University, Oxford, UK, and accepted by Editorial Board Member Zachary Fisk June 29, 2018 (received for review February 28, 2018)

Anomalous surface states with Fermi arcs are commonly considered to be a fingerprint of Dirac semimetals (DSMs). In contrast to Weyl semimetals, however, Fermi arcs of DSMs are not topologically protected. Using first-principles calculations, we predict that β-cuprous iodide (β-CuI) is a peculiar DSM whose surface states form closed Fermi pockets instead of Fermi arcs. In such a fermiological Dirac semimetal, the deformation mechanism from Fermi arcs to Fermi pockets stems from a large cubic term preserving all crystal symmetries and from the small energy difference between the surface and bulk Dirac points. The cubic term in β-CuI, usually negligible in prototypical DSMs, becomes relevant because of the particular crystal structure. As such, we establish a concrete material example manifesting the lack of topological protection for surface Fermi arcs in DSMs.

Dirac semimetals | Weyl semimetals | Fermi arcs | topological insulator

Topological semimetals including Dirac semimetals (DSMs), Weyl semimetals (WSMs), and nodal line semimetals have been attracting enormous attention in contemporary research (1, 2), exhibiting a plethora of exotic phenomena (3–14). In particular, the surface states of such semimetals commonly feature open Fermi arcs rather than closed Fermi pockets (15). The principal existence of Fermi arcs appears robust against potential bulk band hybridizations and has been confirmed by theoretical calculations as well as experimental observations in all type-I and type-II (16) WSM and DSM materials studied so far (17–24).

The topological protection of nondegenerate surface Fermi arcs in WSMs traces back to topological invariants enforcing the connection between Berry flux monopoles of opposite charge, which is realized by pairs of bulk Weyl cones projected to a given surface. In view of DSMs, however, it has been pointed out recently (25, 26) that the doubly degenerate Fermi arcs on side surfaces are not topologically protected and that a cubic term preserving all crystal symmetries can deform Fermi arcs into closed Fermi surfaces, yielding a state we call fermiological DSM. In all DSMs (Na_3Bi and Cd_3As_2) known so far, such a cubic term is negligible, so that doubly degenerate Fermi arcs always appear at the surfaces.

In this work, we predict that β-cuprous iodide (β-CuI) (27, 28) is a proposed instance of a fermiological DSM, exhibiting closed Fermi surfaces instead of Fermi arcs on its side surfaces. The band inversion, which can be greatly enhanced with compressive strain along the c axis, happens between the bonding states of Cu-$4s$ orbitals and I-$5p_{x,y}$ orbitals. It generates both 3D topological semimetal and 3D topological insulator phases. A crystal symmetry-preserving cubic term, which is usually expected to be negligible in previous DSM materials, is found to be considerably larger because of the unique atomic arrangements in β-CuI, in sharp contrast to conventional DSMs such as Na_3Bi and Cd_3As_2. In particular, the small energy difference between surface and bulk Dirac points causes a flat surface state along the Γ–Z direction. In this flat surface state, the cubic term can introduce a gap for $k_z \neq 0$ to deform Fermi arcs into a closed Fermi surface. Our study provides a concrete material example to illustrate the lack of topological protection of surface Fermi arcs in DSMs. The corresponding consequences in angle-resolved photoemission spectroscopy (ARPES) and quantum oscillation measurements are also discussed.

Crystal Structure

The crystal chemistry of CuI is characterized by three stable structural phases α, β, and γ (27). Here, we focus on the topologically nontrivial properties of the β phase. The crystal structure of β-CuI with the space group $R\bar{3}m$ is shown in Fig. 1*A* (27). According to the chemical environment, the I ions can be classified as I_1 and I_2. I_1 is octahedrally coordinated by six Cu atoms, and I_2 is coordinated by only two Cu ions parallel to the c axis, resulting in a strong negative crystal field for the I_1 p orbitals and I_2 p_z orbital. As shown in Fig. 1*A*, the Cu–I_1–Cu form trilayer structures and are connected by I_2 ions along the c axis. In the following calculations, we adopt the experimental structural parameters in ref. 27.

Electronic Structure

The band structure and density of states (DOS) for β-CuI are displayed in Fig. 2. Due to the monovalence of Cu, the d orbitals of Cu are fully filled and located at about −2.5 eV. The p orbitals of I_1 and the p_z orbital of I_2 lie far below the Fermi level because of the strongly negative crystal field. Near the Fermi level, the

Significance

Since the discovery of Dirac semimetals in 3D, open Fermi arcs on side surface terminations have predominantly been suggested to be the concomitant experimental fingerprint of their nontrivial topological character. Surface Fermi arcs, however, are not a protected topological feature of Dirac semimetals, which we predict will manifest itself in the example of β-cuprous iodide. The microscopic mechanism underlying the transition from open Fermi arcs to closed Fermi pockets in this material is explicitly revealed. Our study provides a concise example to show the lack of topological protection of surface Fermi arcs in Dirac semimetals and, as such, deepens the fundamental understanding of topological semimetals in general.

Author contributions: C.L., X.W., and J.H. designed research; C.L. and X.W. performed research; C.L., X.W., S.Q., Y.L., R.T., F.-C.Z., and J.H. analyzed data; and C.L., X.W., S.Q., Y.L., R.T., F.-C.Z., and J.H. wrote the paper.

The authors declare no conflict of interest.

This article is a PNAS Direct Submission. S.P. is a guest editor invited by the Editorial Board.

[1]To whom correspondence may be addressed. Email: xianxinwu@gmail.com or jphu@iphy.ac.cn.

This article contains supporting information online at www.pnas.org/lookup/suppl/doi:10.1073/pnas.1803599115/-/DCSupplemental.

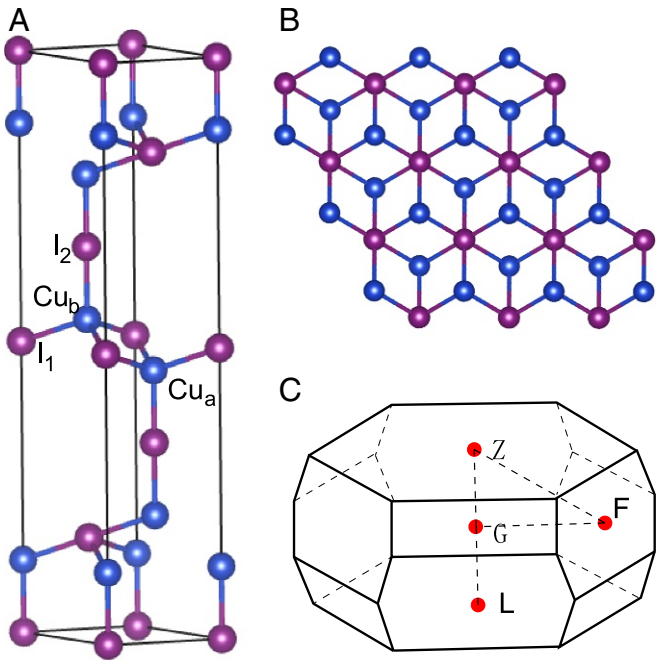

Fig. 1. Crystal structure and primitive Brillouin zone for β-CuI. (*A*) Crystal structure of β-CuI. Cu–I_1–Cu trilayers stacking along the *c* axis are connected by I_2 ions. (*B*) Top view of crystal structure of Cu–I_1–Cu trilayers. I_1 is octahedrally coordinated by six Cu atoms, which generate a negative crystal field. (*C*) Primitive Brillouin zone for β-CuI.

valence and conduction bands are predominantly attributed to the I_2-5$p_{x/y}$ and Cu-4s orbitals. The most prominent feature in the band structure is that at the Γ point, the Cu-4s band is lower than the I-5$p_{x,y}$ bands by about 0.47 eV and that there is a crossing point along the ΓZ line near the Fermi level, as shown in Fig. 2*A*. Due to strong spin orbital coupling (SOC) in I ions, we further take SOC into consideration in our calculations. As shown in Fig. 2*C*, the I-5$p_{x,y}$ bands in the ΓZ line split into $\Lambda_5 + \Lambda_6$ ($|j_z = \pm\frac{3}{2}\rangle$) and Λ_4 ($|j_z = \pm\frac{1}{2}\rangle$) bands, and the band inversion at the Γ point is further enhanced to 0.77 eV. As the generalized gradient approximation occasionally tends to underestimate band gaps, we further assert the avenue of band inversion by hybrid functional Heyd–Scuseria–Ernzerhof calculations and also find that the gap can be greatly enhanced through compressive strain along the c axis (*SI Appendix*, section 2). Furthermore, as the two crossing bands along the ΓZ line belong to different irreducible representations as distinguished by C_3 rotational symmetry around the z axis, this indicates that the 3D Dirac cones near the Fermi level are stable. Notably, the Cu-4s and I-5$p_{x,y}$ $|j_z = \pm\frac{1}{2}\rangle$ bands have the same Λ_4 irreducible representation, which leads to a band anticrossing and a full gap opening around -0.4 eV. As the parities of Cu-4s and I-5p bands are opposite at the Γ and the Z point, band inversion will drive the system into a topologically nontrivial phase. Due to the presence of 3D inversion symmetry in β-CuI, we can calculate Z_2 topological invariants by analyzing the parity eigenstates at high-symmetry points (29). The parity of the eigenstates near the Fermi level at Γ and Z points is displayed in Fig. 2*C*. According to our calculations, CuI is a topologically nontrivial semimetal, with 3D Z_2 invariants given by $(1;000)$ (*SI Appendix*, section 1). Furthermore, setting the chemical potential to -0.4 eV, the system is located in a topological insulator phase with nontrivial Z_2 invariants. In total, we thus find that band inversion generates both topological semimetal and topological insulator phases.

Because of bulk–edge correspondence, a topologically nontrivial bulk state is accompanied by gapless surface states. For CuI, these can be obtained by calculating the surface Green function of the semiinfinite system through an iterative procedure (30, 31). Fig. 3*A* shows the edge states on the (001) surface. Interestingly, a surface Dirac cone exists around -0.4 eV stemming from the nontrivial topological insulator phase, and the corresponding Fermi surface is a closed circle with a left-handed spin texture (*SI Appendix*, section 6). The surface states of the (100) surface in the conventional cell are shown in Fig. 3*B*. The energy difference Δ between the surface Dirac point at Γ and the projections of the bulk Dirac points is extremely small, yielding flat surface states along ΓZ, in sharp contrast to conventional DSMs (6, 15) (*SI Appendix*, section 7). Despite the band folding along the ΓZ direction (*SI Appendix*, section 4), we find that the two surface states vanish at the projection of bulk Dirac points and exhibit nonmonotonic dispersion along ΓZ. Furthermore, the lower surface state first sinks below the energy level E_D of the bulk Dirac points, then rises above it, and finally bends down to saturate at it, resulting in three crossing points for $k_y = 0$ at E_D (denoted by white and red circles in Fig. 3 *B* and *D*). The corresponding Fermi surface of (100) surface at E_D is shown in Fig. 3*D*. There is one closed nontrivial Fermi pocket centered around $k_z = 0$ and there are two trivial pockets around $k_z = \pi$, which originate from the nontrivial Z_2 invariant in the $k_z = 0$ plane and the trivial Z_2 invariant in the $k_z = \pi$ plane, respectively. The closed Fermi pocket around $k_z = 0$ does not pass through the projections of the bulk Dirac points (denoted by red circles in Fig. 3*D*), illustrating that Fermi arcs are absent. Furthermore, the surface states at an exemplary amount of $k_z = \pi/6$ lower than the location k_{zD} of the Dirac point, which exhibit gap opening, are shown in Fig. 3*C*. We find that the obtained surface states are gapped for all k_z except $k_z = 0$, which plays an important role in deforming Fermi arcs into a closed Fermi surface.

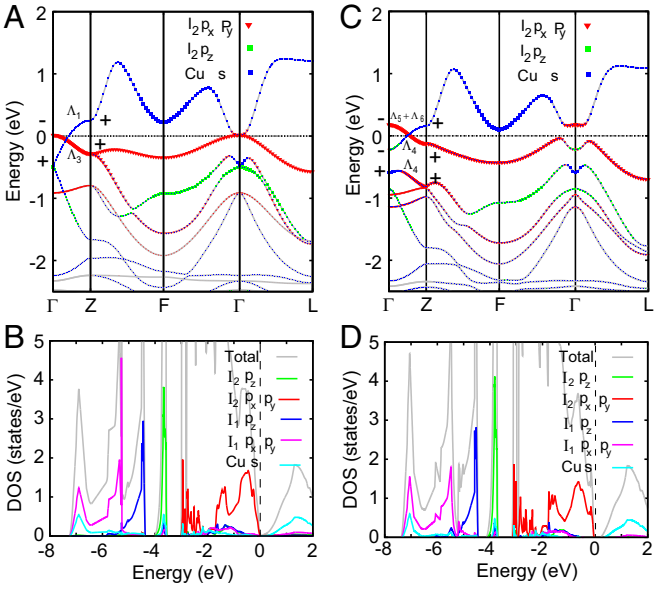

Fig. 2. Band structures and DOS for β-CuI without SOC and with SOC. (*A* and *B*) Band structures and DOS of β-CuI without SOC. The band inversion happens between I_2-5$p_{x/y}$ and Cu-4s orbitals, and Dirac points are located in ΓZ near the Fermi level. (*C* and *D*) Band structures and DOS of β-CuI with SOC. The I-5$p_{x,y}$ bands in the ΓZ line are split, and the band inversion at the Γ point is further enhanced to be 0.77 eV. The orbital weights are represented by the areas of circles and triangles. The parities of the eigenstates and the irreducible representations of bands at the Γ point near the Fermi level are shown. The eigenvalues of C_3 for bands along the Γ–Z line are displayed in *SI Appendix*, section 1.

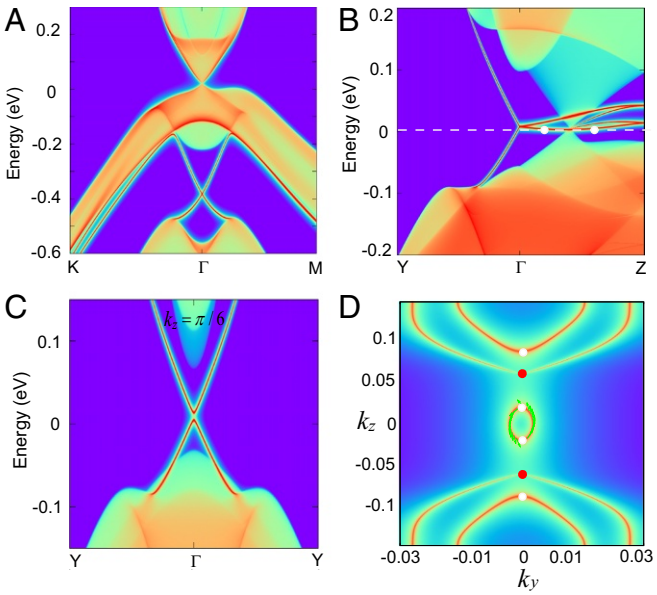

Fig. 3. The (001) and (100) surface states and Fermi surfaces for β-CuI. (*A* and *B*) Projected surface states of β-CuI for (001) and (100) surfaces in the conventional cell. On the (001) surface a surface Dirac cone exists around −0.4 eV and on the (100) surface the two surface states exhibit nonmonotonic dispersion along ΓZ and vanish at the projection of bulk Dirac points. (*C*) Projected surface states of β-CuI for the (100) surface at the $k_z = \frac{\pi}{6}$ plane, where surface states are gapped. (*D*) Fermi surface at the energy of bulk Dirac points for the (100) surface. One closed nontrivial Fermi pocket with spin helical texture (shown by green arrows) is centered around $k_z = 0$. The closed pocket does not pass through the projections of the bulk Dirac points (red circles), illustrating that Fermi arcs are absent.

Effective Hamiltonian

To characterize the low-energy effective Hamiltonian around the Γ point, which is helpful to understand the origin of the surface Fermi arc breakdown, we adopt the perspective of the theory of invariants (32). From the band structure, the states around Γ are mainly attributed to I$_2$-5$p_{x,y}$ and Cu-4s orbitals, and thus these orbitals can be used to construct the basis. Further considering the inversion symmetry in the system, it is convenient to combine these orbitals to form the eigenstates of the inversion symmetry, which are given by

$$\begin{aligned}\left|P_\alpha^\pm\right\rangle &= \frac{1}{\sqrt{2}}\left(\left|\mathrm{I}_\alpha\right\rangle \pm \left|\mathrm{I}'_\alpha\right\rangle\right),\\ \left|S^\pm\right\rangle &= \frac{1}{\sqrt{2}}\left(\left|\mathrm{Cu}_s\right\rangle \pm \left|\mathrm{Cu}'_s\right\rangle\right),\end{aligned} \qquad [1]$$

where the superscript denotes the parity, $\alpha = p_{x,y}$, and the I (Cu) as well as I′ (Cu′) atoms are related by inversion symmetry. We focus on the low-energy states near the bulk Dirac point. After further taking into account SOC in the atomic picture, we can choose $\left|S^+, \frac{1}{2}\right\rangle$, $\left|P^-, \frac{3}{2}\right\rangle$, $\left|S^+, -\frac{1}{2}\right\rangle$, $\left|P^-, -\frac{3}{2}\right\rangle$ as the basis in $\mathbf{k}\cdot\mathbf{p}$ theory to construct the effective Hamiltonian around the Γ point. The Hamiltonian to third order in $\mathbf{k}$ reads

$$\begin{aligned}H_{eff}(\mathbf{k}) &= H_0 + H_1 + H_2\\ H_0 &= \epsilon(\mathbf{k}) + M(\mathbf{k})\sigma_0\tau_3 - A(\mathbf{k}_\parallel)(k_x\sigma_3\tau_2 + k_y\sigma_0\tau_1)\\ H_1 &= (D_2 + D_3k_z^2)(-k_x\sigma_1\tau_2 + k_y\sigma_2\tau_2)\\ H_2 &= -D_1k_z[(k_x^2 - k_y^2)\sigma_1\tau_2 + 2k_xk_y\sigma_2\tau_2],\end{aligned} \qquad [2]$$

where the Pauli matrices σ act in spin and τ in orbital space, $k_\pm = k_x \pm ik_y$, $\epsilon_{\mathbf{k}} = C_0 + C_1k_z^2 + C_2(k_x^2 + k_y^2)$, $M(\mathbf{k}) = M_0 - M_1k_z^2 - M_2(k_x^2 + k_y^2)$, $A(\mathbf{k}_\parallel) = A_0 + A_1k_z^2$, $D(\mathbf{k}) = ik_+(D_2 + D_3k_z^2)$, and $\tilde{D}(\mathbf{k}) = iD_1k_zk_-^2$. The antidiagonal terms contain first-order and third-order terms, which have often been omitted in previous studies, but turn out to be of great importance in β-CuI. The energy dispersion of the Hamiltonian for the DSM is $E(k) = \epsilon_{\mathbf{k}} \pm \sqrt{M(\mathbf{k})^2 + A^2k_+k_- + \left|D(\mathbf{k}) + \tilde{D}(\mathbf{k})\right|^2}$, resulting in two band crossing points (0,0, $\pm k_{zD}$) along the Γ–Z line with $k_{zD} = \sqrt{\frac{M_0}{M_1}}$. By fitting the bands of the effective model with those of density functional theory (DFT) calculation around the Γ point, the parameters in the effective model are given by $C_0 = -0.2070$ eV, $C_1 = 2.0445$ eV·Å^2, $C_2 = 12.8481$ eV·Å^2, $M_0 = -0.3855$ eV, $M_1 = -6.8288$ eV·Å^2, $M_2 = -37.4544$ eV·Å^2, $A_0 = 4.0035$ eV·Å, $A_1 = -1{,}629.0242$ eV·Å^2, $D_1 = 167.799$ eV·Å^3, $D_2 = 2.8549$ eV·Å, and $D_3 = -1{,}668.6306$ eV·Å^3. In β-CuI, we find that the coefficients in the antidiagonal terms are considerably large and thus cannot be omitted.

In ref. 25, the Fermi arcs on the (100) surface have been shown to be not protected by symmetry and can in principle be absent. Still, the effective Hamiltonian H_0, up to second order in $\mathbf{k}$, can give robust surface Fermi arcs. Therefore, H_0 must have additional symmetries, which are to some degree artificial and not enforced for DSM materials. Consider a pseudo–time-reversal symmetry $\mathcal{T}$ in 2D, which can be defined as $\mathcal{T} = i\sigma_2\tau_3 \cdot K$. Under this operation, the Hamiltonian for $H(k_x, k_y, k_{z_0})$ at a fixed k_{z_0} plane transforms as $\mathcal{T}H(k_x, k_y, k_{z_0})\mathcal{T}^{-1} = H(-k_x, -k_y, k_{z_0})$. It can be easily verified that the Hamiltonians H_0 and H_1 are invariant under the operation $\mathcal{T}$. This symmetry, not preserved for the generic realistic system but only for the Hamiltonian H_0, H_1, and its side surfaces, can protect gapless surface states for any $k_z < k_{z_D}$ planes. The energy difference between the surface Dirac point and the bulk Dirac point is given by (*SI Appendix*, section 5)

$$\Delta = \left(\frac{C_2}{M_2} - \frac{C_1}{M_1}\right)M_0. \qquad [3]$$

The corresponding prototypical surface states on the (100) surface along Y–Γ–Z for $H_0 + H_1$, with a small Δ, are shown in Fig. 4*A*, where the energy of two degenerate flat surface states decreases monotonically with increasing momentum along ΓZ. As a consequence of the latter, there are only two points in $k_y = 0$ on the Fermi surface at E_D, that is, the projected bulk Dirac points, and Fermi arcs can robustly appear on the (100) surface. It is, however, the cubic H_2 term that breaks this artificial symmetry and naturally introduces gap openings for any k_z except $k_z = 0$ where fundamental time-reversal symmetry is kept. Taking H_2 into consideration, two surface states split, as shown in Fig. 4*B*, and the prominent feature is that both surface states exhibit a nonmonotonic band dispersion along Γ–Z, which generates an additional two points in $k_y = 0$ at E_D in the surface state. As such, the Fermi arcs deform into a closed Fermi pocket, bearing some similarity to a 3D topological insulator surface state. Further increasing coefficients in H_1, we find that this will reduce the splitting of surface states along Γ–Z. Adding either inversion symmetry or time-reversal symmetry breaking, DSMs become WSMs, and Fermi arcs are known to be robust (*SI Appendix*, section 7). In the presence of both these symmetries, however, the cubic term explicates how Fermi arcs on the surface of a DSM are not topologically protected.

We now turn to a detailed analysis of why despite the above finding, the hallmark of DSM materials discovered previously, such as Na_3Bi and Cd_3As_2, still has the appearance of seemingly robust Fermi arcs. We conjecture that this is attributed to a small

PHYSICS

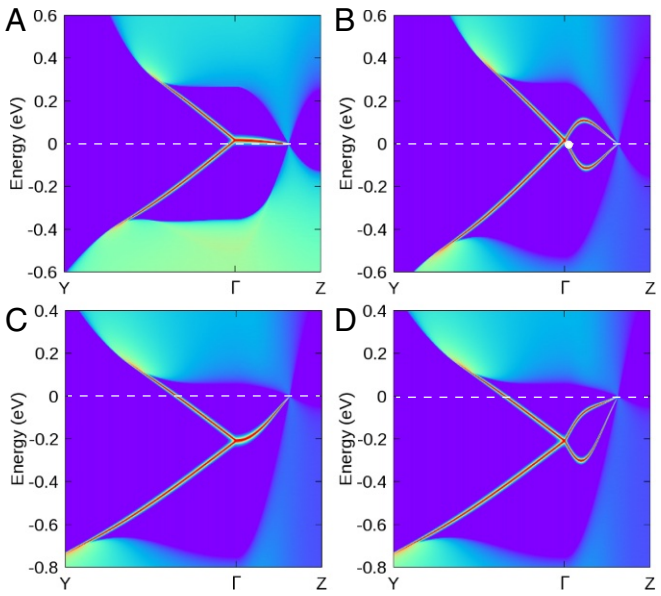

Fig. 4. The (100) surface states from the effective Hamiltonian with different D_1 and Δ. (*A* and *B*) Calculated (100) surface states from H_0+H_1 (*A*) and $H_0+H_1+H_2$ (*B*) with a small Δ. Taking H_2 into consideration, the Fermi arcs deform into a closed Fermi pocket. (*C* and *D*) Calculated surface states from H_0+H_1 (*C*) and $H_0+H_1+H_2$ (*D*) with a large Δ. The effect of the cubic term is weakened due to the large Δ and Fermi arcs can still exist. Both the large cubic term and small Δ are crucial to the absence of side Fermi arcs in DSMs.

coefficient of the cubic term in H_2 along with a large Δ. How does this change for β-CuI? We start by analyzing the origin of the H_2 term, which corresponds to the coupling of $\left|P^-,\frac{3}{2}\right\rangle$ and $\left|S^+,-\frac{1}{2}\right\rangle$. The only process generating this coupling in β-CuI can be summarized as

$$\left|p^{I_2}_{x/y,\sigma}\right\rangle \xrightarrow{\lambda_I} \left|p^{I_2}_{z,\bar{\sigma}}\right\rangle \xrightarrow{t_1} \left|s^{Cu_b}_{\bar{\sigma}}\right\rangle \xrightarrow{t_2} \left|s^{Cu_a}_{\bar{\sigma}}\right\rangle, \qquad [4]$$

where $\sigma=\uparrow,\downarrow$ labels the spin. The hybridization process is as follows: First, $\left|p^{I_2}_{x/y,\sigma}\right\rangle$ couples strongly with $\left|p^{I_2}_{z,\bar{\sigma}}\right\rangle$ due to strong atomic SOC in I atoms; as there is a strong σ bond between I_2 and Cu_b, $\left|p^{I_2}_{z,\bar{\sigma}}\right\rangle$ can strongly hybridize with $\left|s^{Cu_b}_{\bar{\sigma}}\right\rangle$; because of the short distance between Cu_a and Cu_b, $\left|s^{Cu_a}_{\bar{\sigma}}\right\rangle$ and $\left|s^{Cu_b}_{\bar{\sigma}}\right\rangle$ exhibit considerable coupling; and finally, the $\left|P^-,\frac{3}{2}\right\rangle$ can couple indirectly via $\left|S^+,-\frac{1}{2}\right\rangle$, and the coupling constant D_1 is proportional to $\lambda_I t_1 t_2$. In β-CuI, all three parameters are large, and hence they generate a considerable D_1. While the microscopic mechanism explained above is derived for a specific material, it potentially applies to a series of other DSMs, certainly to the ones originating from band inversion between $\left|j_z=\pm\frac{3}{2}\right\rangle$ and $\left|j_z=\pm\frac{1}{2}\right\rangle$ states with opposite parities. In Na_3Bi and Cd_3As_2, even though SOC is even stronger than for CuI, the second and third steps of the process are considerably weakened because of the weak bonding between cations and anions, indicating that the D_1 parameter is small there. In addition, Δ in Na_3Bi is much larger than that in β-CuI, which also weakens the effect of the cubic term. Fig. 4*C* shows the surface states with a large Δ, where surface states exhibit a large dispersion along Γ–Z. Including the same cubic term as in Fig. 4*D*, the band splitting weakens, and Fermi arcs can still exist in this case. Thus, small Δ is another prerequisite to impose on the absence of Fermi arcs. The H_1 term in β-CuI preserves $\mathcal{T}$ symmetry and, if dominant, can substantially suppress the gap opening for the surface states. The first term in $D(k)$, however, involves only in-plane coupling, and is weak because of no immediate microscopic foundation in real space; the second term includes k_z^2 and, as such, in comparison with H_2 has a much weaker effect for small k_z. Therefore, the combined appearance of large D_1 as well as small Δ in β-CuI triggers the breakdown of surface Fermi arcs.

Discussion

We elaborate on experimental evidence derived from the breakdown of surface Fermi arcs due to a significant cubic term. First, aiming at the effect of the cubic term in the bulk, the in-plane energy dispersion for a specific k_z is $E(k)=\epsilon_{\mathbf{k}}\pm\sqrt{f_1+f_2|k|^2+f_3|k|^4}$. If D_1 is large, the coefficient $f_3=M_2^2+D_1^2k_z^2$ should exhibit noticeable k_z dependence, which could be identified upon fitting the band structure against ARPES measurements. Second, as the splitting of (100) surface states along Γ–Z is directly related to the cubic term, this splitting can likewise be obtained in ARPES and is expected to be relatively large as well as strongly k_z dependent. In addition, the change of nature of the surface states from arcs to closed Fermi pockets hints at immediate experimental implications. First, terminating Fermi arcs and closed Fermi surfaces exhibit qualitative differentiable shape differences in ARPES measurements. For the former, when two Fermi arcs meet at the projection of bulk Dirac points, there is a singular change in slope, whereas for the latter, the closed Fermi surface has a smooth curvature everywhere and does not pass through the projections of bulk Dirac points. Second, the distinct behavior of surface Fermi arcs vs. closed surface Fermi pockets in quantum oscillation measurements can be used to contrast them. In the former case, the quantum oscillation frequency F_s is strongly dependent on the sample thickness due to the Weyl orbits (33, 34). In triangle-shaped samples, quantum oscillations can be even unobservable in experiment (34). In the latter case, fermions acquire a measurable Berry phase of π as they encircle the Fermi contour, similar to topological insulators. In contrast to the former case, quantum oscillations can exist in triangle-shaped samples (35–37) and exhibit weak thickness dependence.

Conclusion

Based on first-principles calculations we predict that β-CuI is a topological unconventional DSM exhibiting closed Fermi surfaces instead of Fermi arcs on its side surfaces. The theoretical discovery of β-CuI provides explicit proof that the Fermi arcs in DSMs are not topologically protected. Our study also suggests that halide compounds can be a fertile ground to explore novel topological properties.

Methods

Our calculations are performed using DFT as implemented in the Vienna ab initio simulation package (VASP) code (38–40). The Perdew–Burke–Ernzerhof (PBE) exchange-correlation functional and the projector–augmented-wave (PAW) approach are used. Throughout this work, the cutoff energy is set to 500 eV for expanding the wave functions into plane-wave basis. In the calculation, the Brillouin zone is sampled in the k space within the Monkhorst–Pack scheme (41). On the basis of the equilibrium structure, the k mesh used is $6\times6\times6$ and $10\times10\times2$ for primitive and conventional cells, respectively.

ACKNOWLEDGMENTS. We thank Chen Fang and Lunhui Hu for helpful discussion. This work is supported by the Ministry of Science and Technology of China 973 program (Grants 2015CB921300 and 2017YFA0303100), the National Science Foundation of China (Grant NSFC-11334012), and the Strategic Priority Research Program of Chinese Academy of Sciences (Grant XD-B07000000). This work is supported in part by the Key Research Program of the Chinese Academy of Sciences (Grant XDPB08-4), the Strategic Priority Research Program of Chinese Academy of Sciences (Grant XDB28000000), and the National Science Foundation of China (Grant NSFC-11674278). The work in Würzburg is supported by the European Research Council (ERC) through ERC-StG-TOPOLECTRICS-336012 and by the German Research Foundation (DFG) through the special research unit (SFB) DFG-SFB 1170 (Project B04) and through the priority programme (SPP) DFG-SPP 1666.

1. Chiu C-K, Teo JC, Schnyder AP, Ryu S (2016) Classification of topological quantum matter with symmetries. *Rev Mod Phys* 88:035005.
2. Armitage NP, Mele EJ, Vishwanath A (2018) Weyl and Dirac semimetals in three-dimensional solids. *Rev Mod Phys* 90:015001.
3. Xu G, Weng H, Wang Z, Dai X, Fang Z (2011) Chern semimetal and the quantized anomalous Hall effect in $HgCr_2Se_4$. *Phys Rev Lett* 107:186806.
4. Wan X, Turner AM, Vishwanath A, Savrasov SY (2011) Topological semimetal and Fermi-arc surface states in the electronic structure of pyrochlore iridates. *Phys Rev B* 83:205101.
5. Balents L (2011) Weyl electrons kiss. *Physics* 4:36.
6. Wang Z, et al. (2012) Dirac semimetal and topological phase transitions in A_3Bi (A = Na, K, Rb). *Phys Rev B* 85:195320.
7. Wang Z, Weng H, Wu Q, Dai X, Fang Z (2013) Three-dimensional Dirac semimetal and quantum transport in Cd_3As_2. *Phys Rev B* 88:125427.
8. Parameswaran SA, Grover T, Abanin DA, Pesin D, Vishwanath A (2014) Probing the chiral anomaly with nonlocal transport in three-dimensional topological semimetals. *Phys Rev X* 4:031035.
9. Huang X, et al. (2015) Observation of the chiral-anomaly-induced negative magnetoresistance in 3D Weyl semimetal TaAs. *Phys Rev X* 5:031023.
10. Liang T, et al. (2014) Ultrahigh mobility and giant magnetoresistance in the Dirac semimetal Cd_3As_2. *Nat Mater* 14:280.
11. Baum Y, Berg E, Parameswaran S, Stern A (2015) Current at a distance and resonant transparency in Weyl semimetals. *Phys Rev X* 5:041046.
12. Xiong J, et al. (2015) Evidence for the Chiral anomaly in the Dirac semimetal Na_3Bi. *Science* 350:413–416.
13. Weng H, Fang C, Fang Z, Bernevig B, Dai X (2015) Weyl semimetal phase in noncentrosymmetric transition-metal monophosphides. *Phys Rev X* 5:011029.
14. Huang S-M, et al. (2015) A Weyl fermion semimetal with surface Fermi arcs in the transition metal monopnictide TaAs class. *Nat Commun* 6:7373.
15. Xu S-Y, et al. (2015) Observation of Fermi arc surface states in a topological metal. *Science* 347:294–298.
16. Soluyanov AA, et al. (2015) Type-II Weyl semimetals. *Nature* 527:495–498.
17. Chang T-R, et al. (2017) Type-II symmetry-protected topological Dirac semimetals. *Phys Rev Lett* 119:026404.
18. Huang H, Zhou S, Duan W (2016) Type-II Dirac fermions in the $PtSe_2$ class of transition metal dichalcogenides. *Phys Rev B* 94:121117.
19. Yan M, et al. (2017) Lorentz-violating type-II Dirac fermions in transition metal dichalcogenide $PtTe_2$. *Nat Commun* 8:257.
20. Noh H-J, et al. (2017) Experimental realization of type-II Dirac fermions in a $PdTe_2$ superconductor. *Phys Rev Lett* 119:016401.
21. Fei F, et al. (2017) Nontrivial Berry phase and type-II Dirac transport in the layered material $PdTe_2$. *Phys Rev B* 96:041201.
22. Le C, et al. (2017) Three-dimensional topological critical Dirac semimetal in AMgBi (A = K, Rb, Cs). *Phys Rev B* 96:115121.
23. Gorbar EV, Miransky VA, Shovkovy IA, Sukhachov PO (2015) Dirac semimetals A_3Bi (a = Na, K, Rb) as Γ_2 Weyl semimetals. *Phys Rev B* 91:121101.
24. Gorbar EV, Miransky VA, Shovkovy IA, Sukhachov PO (2015) Surface Fermi arcs in Γ_2 Weyl semimetals A_3Bi (a = Na, k, rb). *Phys Rev B* 91:235138.
25. Kargarian M, Randeria M, Lu Y-M (2016) Are the surface Fermi arcs in Dirac semimetals topologically protected? *Proc Natl Acad Sci USA* 113:8648–8652.
26. Kargarian M, Lu Y-M, Randeria M (2018) Deformation and stability of surface states in Dirac semimetals. *Phys Rev B* 97:165129.
27. Shan Y, et al. (2009) Description of the phase transitions of cuprous iodide. *J Alloys Compd* 477:403–406.
28. Keen DA, Hull S (1995) The high-temperature structural behaviour of copper(I) iodide. *J Phys Condensed Matter* 7:5793–5804.
29. Fu L, Kane CL (2007) Topological insulators with inversion symmetry. *Phys Rev B* 76:045302.
30. López Sancho MP, López Sancho JM, Rubio J (1984) Quick iterative scheme for the calculation of transfer matrices: Application to Mo (100). *J Phys F* 14:1205–1215.
31. Lopez Sancho MP, Lopez Sancho JM, Lopez Sancho JM, Rubio J (1985) Highly convergent schemes for the calculation of bulk and surface Green functions. *J Phys F* 15:851–858.
32. Liu C-X, et al. (2010) Model Hamiltonian for topological insulators. *Phys Rev B* 82:045122.
33. Potter AC, Kimchi I, Vishwanath A (2014) Quantum oscillations from surface Fermi arcs in Weyl and Dirac semimetals. *Nat Commun* 5:5161.
34. Moll PJW, et al. (2016) Transport evidence for Fermi-arc-mediated chirality transfer in the Dirac semimetal Cd_3As_2. *Nature* 535:266–270.
35. Ren Z, Taskin AA, Sasaki S, Segawa K, Ando Y (2010) Large bulk resistivity and surface quantum oscillations in the topological insulator bi_2te_2Se. *Phys Rev B* 82:241306.
36. Qu D-X, Hor YS, Xiong J, Cava RJ, Ong NP (2010) Quantum oscillations and Hall anomaly of surface states in the topological insulator Bi_2Te_3. *Science* 329:821–824.
37. Analytis JG, et al. (2010) Two-dimensional surface state in the quantum limit of a topological insulator. *Nat Phys* 6:960–964.
38. Kresse G, Hafner J (1993) Ab initio molecular dynamics for liquid metals. *Phys Rev B* 47:558–561.
39. Kresse G, Furthmüller J (1996) Efficiency of ab-initio total energy calculations for metals and semiconductors using a plane-wave basis set. *Comput Mater Sci* 6: 15–50.
40. Kresse G, Furthmüller J (1996) Efficient iterative schemes for ab initio total-energy calculations using a plane-wave basis set. *Phys Rev B* 54:11169–11186.
41. Monkhorst HJ, Pack JD (1976) Special points for Brillouin-zone integrations. *Phys Rev B* 13:5188–5192.